The Astrophysical Journal, 878:136 (14pp), 2019 June 20 https://doi.org/10.3847/1538-4357/ab1f66

Confirmation of the *Gaia* DR2 Parallax Zero-point Offset Using Asteroseismology and Spectroscopy in the *Kepler* Field

Joel C. Zinn[1], Marc H. Pinsonneault[1], Daniel Huber[2,3,4,5], and Dennis Stello[3,4,6,7]
[1] Department of Astronomy, The Ohio State University, 140 West 18th Avenue, Columbus OH 43210, USA; zinn.44@osu.edu
[2] Institute for Astronomy, University of Hawai'i, 2680 Woodlawn Drive, Honolulu, HI 96822, USA
[3] Sydney Institute for Astronomy (SIfA), School of Physics, University of Sydney, NSW 2006, Australia
[4] Stellar Astrophysics Centre, Department of Physics and Astronomy, Aarhus University, Ny Munkegade 120, DK-8000 Aarhus C, Denmark
[5] SETI Institute, 189 Bernardo Avenue, Mountain View, CA 94043, USA
[6] School of Physics, University of New South Wales, Barker Street, Sydney, NSW 2052, Australia
[7] Center of Excellence for Astrophysics in Three Dimensions (ASTRO-3D), Australia
Received 2018 May 7; revised 2019 April 19; accepted 2019 May 3; published 2019 June 21

Abstract

We present an independent confirmation of the zero-point offset of *Gaia* Data Release 2 parallaxes using asteroseismic data of evolved stars in the *Kepler* field. Using well-characterized red giant branch stars from the APOKASC-2 catalog, we identify a *Gaia* astrometric pseudocolor ($\nu_{\rm eff}$)- and *Gaia* *G*-band magnitude-dependent zero-point offset of $\varpi_{\rm seis} - \varpi_{Gaia} = 52.8 \pm 2.4$ (rand.) $\pm$ 8.6 (syst.) $-$ $(150.7 \pm 22.7)(\nu_{\rm eff} - 1.5) - (4.21 \pm 0.77)(G - 12.2)$ μas, in the sense that *Gaia* parallaxes are too small. The offset is found in high- and low-extinction samples, as well as among both shell H-burning red giant stars and core He-burning red clump stars. We show that errors in the asteroseismic radius and temperature scales may be distinguished from errors in the *Gaia* parallax scale. We estimate systematic effects on the inferred global *Gaia* parallax offset, *c*, due to radius and temperature systematics, as well as choices in bolometric correction and the adopted form for *Gaia* parallax spatial correlations. Because of possible spatially correlated parallax errors, as discussed by the *Gaia* team, our *Gaia* parallax offset model is specific to the *Kepler* field, but broadly compatible with the magnitude- and color-dependent offset inferred by the *Gaia* team and several subsequent investigations using independent methods.

Key words: asteroseismology – catalogs – parallaxes – stars: distances

1. Introduction

The recent release of *Gaia* astrometry as part of Data Release 2 (DR2; Gaia Collaboration et al. 2016, 2018) signals an unprecedented opportunity to test stellar astrophysics. In particular, the parallaxes—with typical formal precisions of 0.03 mas for sources with $G > 15$ (Lindegren et al. 2018; hereafter L18)—can be used to solve one of the greatest and most challenging problems in stellar astrophysics, namely the determination of distances. At small parallax, however, the results become sensitive to systematic errors, and checks from alternative techniques are valuable. In this paper we use asteroseismic data to test zero-point offsets in the *Gaia* parallaxes.

The first data release of *Gaia*, using the Tycho-*Gaia* astrometric solution (TGAS; Michalik et al. 2015; Gaia Collaboration et al. 2016), represented a significant advance over the earlier *Hipparcos* work (van Leeuwen 2007). However, the TGAS investigators did note the existence of both spatial correlations and a zero-point offset (Lindegren et al. 2016). Their work was confirmed by other investigators. For the closest objects, Jao et al. (2016) and Stassun & Torres (2016) found consistent offsets of $\approx$0.2 mas in the sense that TGAS parallaxes were too small when compared to trigonometric parallaxes for 612 dwarfs with parallaxes greater than 10 mas and 111 eclipsing binaries with parallaxes mostly greater than 1 mas. Comparing these results for relatively nearby stars to results from more distant giants with parallaxes of less than 1 mas derived from *Kepler* data (Borucki et al. 2010) indicated the presence of a fractional zero-point offset (De Ridder et al. 2016; Davies et al. 2017; Huber et al. 2017). Indeed, at larger distances than the *Kepler* giant samples, Sesar et al. (2017) found RR Lyrae parallaxes to show no indications of an offset with TGAS parallaxes, and neither did Casertano et al. (2017) based on a sample of Cepheid parallaxes.

There were also follow-up tests of spatially correlated parallaxes after the publication of TGAS. Jao et al. (2016) confirmed these spatial correlations in pointing out parallax offsets between hemispheres. Casertano et al. (2017) later reported evidence for spatial correlations in the parallax error below 10°. Using a larger sample, Zinn et al. (2017) mapped out the spatial correlation of the errors in the *Kepler* field below 10° using asteroseismic distances of $\sim$1400 giants, which showed correlations that increased at subdegree scales.

Systematic errors in the *Gaia* parallaxes exist as well. Indications are that a zero-point error might best be explained by a degeneracy in the astrometric solution between a global parallax shift and a term describing a periodic variation in the spacecraft's basic angle[8] with a period of the spacecraft spin period (L18). A smaller contribution might arise from smearing of the point-spread function (PSF) in the across-scan direction (L18). As part of the DR2 release, Arenou et al. (2018) inferred several estimates of a zero-point offset by comparing the *Gaia* DR2 parallaxes to parallaxes of dwarf galaxies, classical pulsators, stars in spectroscopic surveys, and open and globular clusters (see their Table 1). The zero-point offset does vary among these sources, from 10 to 100 μas, which may represent genuine variation as a function of position on the sky, magnitude, or color, or various systematic errors in the comparison parallaxes.

Independent follow-up points to a similar magnitude for the parallax zero-point systematic error. Riess et al. (2018)

[8] The angle between the two fields of view of *Gaia* that allows an absolute measure of parallax. See Gaia Collaboration et al. (2016) for a review of the mission design.

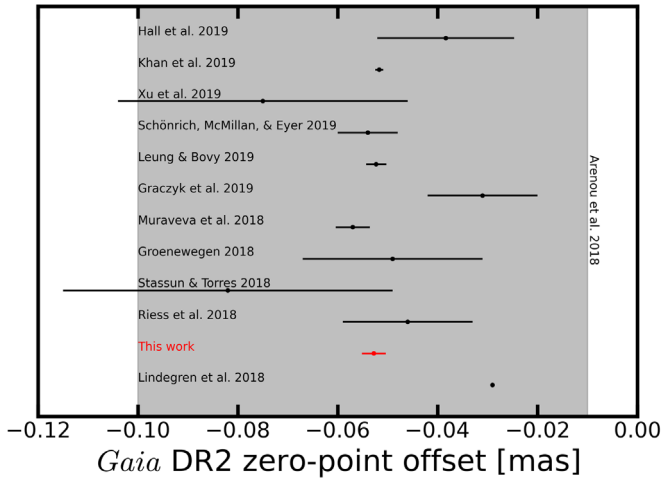

Figure 1. *Gaia* zero-point offsets from the literature, and their statistical uncertainties. No uncertainty was given for the L18 result. The gray band indicates the range of the offset found by Arenou et al. (2018). See the text for details.

confirmed a global offset of 46 ± 11 μas for parallaxes in *Gaia* by comparing *Gaia* parallaxes to those of a sample of 50 Cepheids, whose distances can be precisely determined using a period–luminosity relation. This particular sample is redder and brighter than the sample of quasars used in L18 to test the parallax systematics, and may indeed have a genuinely different zero-point error due to trends in parallax offsets with color and magnitude noted in L18. Also using classical cepheids, Groenewegen (2018) determined a zero-point of 49 μas ± 18 μas, consistent with that of Riess et al. (2018). Muraveva et al. (2018) similarly estimated a mean zero-point offset of 57 μas ± 3.4 μas using three different RR Lyrae absolute magnitude relations.[9] Stassun & Torres (2018) reported a global offset of 82 ± 33 μas when comparing to a sample of 89 eclipsing binaries with dynamical radii. Working with empirical eclipsing binary surface brightness–color relations, Graczyk et al. (2019) estimated a zero-point offset of 31 μas ± 11 μas. Other results confirm this picture: using a statistical approach based on the effect of parallax errors on tangential velocities, Schönrich et al. (2019) determined a zero-point offset of 54 μas ± 6.0 μas; applying a machine-learning distance classifier using APOGEE spectroscopy, Leung & Bovy (2019) found a zero-point offset of 52.3 μas ± 2.0 μas; and Xu et al. (2019) inferred an offset of 75 μas ± 29 μas with very long baseline interferometry astrometry. Most recently, Khan et al. (2019) and Hall et al. (2019) found offsets of 51.7 μas ± 0.8 μas (±≈10 μas when including spatially correlated parallax errors) and $38.38^{+13.54}_{-13.83}$ μas, by computing asteroseismic parallaxes for *Kepler* red giant branch (RGB) and red clump (RC) stars, respectively. All these results are in a consistent direction, in the sense that *Gaia* DR2 parallaxes are too small, and combined, they yield a mean inferred offset of 53.6 μas and a variance-weighted mean of 51.9 μas. We show these zero-point estimates from the literature in Figure 1.

The *Gaia* team has quantified the parallax error budget in DR2 using almost 600,000 quasars from AllWISE (Secrest et al. 2015). They estimate both a global zero-point error of 29 μas (in the sense that *Gaia* parallaxes are too small) and a spatial covariance of the parallaxes, which have a typical angular scale of 10° and an error of 10 μas, and which increases exponentially for smaller scales. Crucially, this means that one cannot benefit from a $\sqrt{N}$ reduction in random uncertainties of the parallax. Given these systematics, the *Gaia* team recommends adopting an irreducible systematic error on the parallaxes of ∼0.1 mas that takes into account both zero-point and spatially correlated errors. This recommended systematic error is large enough to marginalize over much of the position-, color-, and magnitude-dependent nature of the systematics, and in that sense is likely larger than the systematics particular to a specific data set and region of the sky.

Because of the large body of research performed in the *Kepler* field, it is of great interest to quantify the particular systematic errors among its giant population. Here, we quantify a zero-point offset with a sample of nearly 3500 giants with precise asteroseismic distances in the *Kepler* field that also have *Gaia* parallaxes.

2. Data

2.1. The Asteroseismic Comparison Sample

Solar-like oscillations have been detected in thousands of evolved stars by the *CoRoT* and *Kepler* missions (De Ridder et al. 2009; Hekker et al. 2009; Bedding et al. 2010; Stello et al. 2013; Yu et al. 2018). The overall properties of the oscillation frequencies can be characterized by two global measurements: the frequency of maximum power, $\nu_{\rm max}$, and the large frequency spacing, $\Delta\nu$. The observed frequency of maximum power is related to both the surface gravity and $T_{\rm eff}$ (Brown et al. 1991; Kjeldsen & Bedding 1995), while it can be demonstrated that the square of $\Delta\nu$ is proportional to the mean density in the limiting case of homology and large radial order, n (Ulrich 1986). We can therefore solve for stellar mass and radius separately through the usage of scaling relations, typically measured relative to the Sun, if we have asteroseismic data and a robust effective temperature indicator.

Asteroseismic distance estimates are then possible because the combination of radius and $T_{\rm eff}$ yields a luminosity. When combined with an apparent magnitude, an appropriate set of bolometric corrections, and an extinction, the distance can be derived. Fortunately, all of these quantities are well measured in the *Kepler* field.

The basis of our data set is a sample of 6676 *Kepler* red giants with asteroseismic and spectroscopic data taken from Pinsonneault et al. (2018), hereafter APOKASC-2. The APOKASC-2 study provides asteroseismic evolutionary state classification, masses, radii, and extinction measures in the V band. Of particular importance is that the asteroseismic radii are verified to be on an absolute scale by calibrating against fundamental data in star clusters, with typical random uncertainties in radius of under 2% and well-controlled systematics. This means that our asteroseismic distances will also be on a fundamental scale, which is ultimately tied to dynamical open cluster masses.

As a complement to the asteroseismic information, uniform spectroscopic data are available from the APOGEE survey of the Sloan Digital Sky Survey (SDSS) in the *Kepler* field. Almost all of the asteroseismic targets have photometry from 2MASS (Skrutskie et al. 2006), *WISE* (Wright et al. 2010), and *griz* photometry from the *Kepler* Input Catalog (Brown et al. 2011) as corrected by Pinsonneault et al. (2012) to be on the

[9] The uncertainty has been calculated from the standard deviation of the three methods used in Muraveva et al. (2018).

SDSS system, and for which uncertainties are estimated to be 1% in g and r. The spectroscopic $T_{\rm eff}$ values from APOGEE that we use are calibrated to be in agreement with the infrared flux method (IRFM) photometric scale of González Hernández & Bonifacio (2009) for targets in low-extinction fields. The extinctions are well studied in the *Kepler* fields because they can be inferred by requiring consistency between photometric and spectroscopic temperature estimates: extinction will redden photometry of an individual star, biasing its photometric temperature, so an extinction may be derived by adjusting the reddening until the photometric and spectroscopic temperatures agree (see Rodrigues et al. 2014, for details on Bayesian fitting of the extinctions used in the APOKASC-2 catalog).

The masses and radii of shell H-burning (hereafter RGB) stars in the APOKASC-2 catalog are computed using asteroseismic scaling relations, with reference values of $\nu_{\rm max,\odot} = 3076\,\mu$Hz, $\Delta\nu_\odot = 135.146\,\mu$Hz, and $T_{\rm eff,\odot} = 5772$ K. APOKASC-2 uses theoretically motivated corrections to the $\Delta\nu$ scaling relation (e.g., White et al. 2011; Sharma et al. 2016), which induce a differential change between the radii and masses of RGB stars and core He-burning, or RC, stars. As a result, it is important to analyze RGB and RC stars separately, as there are known effects that can produce relative offsets between the two populations (e.g., Miglio et al. 2012). The relative radii of both are consistent with one another in open clusters in the *Kepler* field, but differences at the few percent level could not be ruled out using those samples alone. Our basic sample therefore consists of 3475 RGB stars and 2587 RC stars that pass the *Gaia* DR2 selection cuts as described below. Unless otherwise noted, we only use first-ascent red giants in our main analysis because the APOKASC-2 radii are directly calibrated against RGB stars in open clusters, and because of their larger dynamic range in parameter space—radius and luminosity, in particular—compared to RC stars.

2.2. *The* Gaia *DR2 Sample*

The DR2 catalog contains a host of useful astrometric, photometric, and derived quantities for our purposes. As described in Lindegren et al. (2012), the global *Gaia* astrometric solution is an iterative process that proceeds in stages: first, the astrometric quantities for each star—including the parallaxes, ϖ_{Gaia}, that we use in this work—are updated by minimizing the difference between the observed and predicted locations of the source images on the detector; next, the parameters describing the pointing of the *Gaia* satellite are updated; then the calibration solution is improved, which describes how the observed positions of the sources are systematically affected by instrumental effects like CCD irregularities, mechanical variations, and thermal fluctuations.[10]

Chromatic effects can affect the position of a source on the detector, meaning that there are generally color-dependent offsets in the observed position of a star on the detector that should be accounted for in the calibration part of the solution. Although not a part of the *Gaia* DR1 calibration solution, the global astrometric solution described in DR2 includes an additional term in the calibration step of the solution that depends on a proxy for color, $\nu_{\rm eff}$. This quantity is the inverse of the effective wavenumber of a star, and depends on its spectral shape. $\nu_{\rm eff}$ would normally be computed through an effective wavenumber-color relation using $G_{\rm BP}$ and $G_{\rm RP}$, for instance (Equation (2) in L18). However, given an initial calibration solution that describes how chromaticity affects the positions of stars on the detector, $\nu_{\rm eff}$ can be estimated by adding it to the astrometric part of the solution (see Section 3.1 of L18). For stars where a five-parameter astrometric solution is possible, this astrometric pseudocolor is reported in *Gaia* DR2, and has units of inverse micrometers. $\nu_{\rm eff}$ tends to have more information about instrumental effects than would an effective wavenumber computed from photometry, as indicated by observations by Arenou et al. (2018) that parallax systematics correlate more strongly with $\nu_{\rm eff}$ than with *Gaia* color, $G_{\rm BP}$–$G_{\rm RP}$. We therefore use $\nu_{\rm eff}$ as an explanatory factor in our model to describe the offset between asteroseismic and *Gaia* parallaxes.

We also make use of *Gaia* DR2 photometry, including *Gaia* G, and the blue and red bandpass photometry, $G_{\rm BP}$ and $G_{\rm RP}$. The photometry is reduced based on the positions of the sources from the global astrometric solution, and internally calibrated according to Riello et al. (2018).

We only use stars in common with APOKASC-2 and DR2 by matching on 2MASS ID, and from those, only keep those that meet criteria used by Andrae et al. (2018), namely

1. `astrometric_excess_noise` $= 0$
2. `visibility_periods_used` > 8

and with $\chi^2 \equiv$ `astrometric_chi2_al`, $n \equiv$ `astrometric_n_good_obs_al- 5`, $G_{\rm BP} =$ `phot_bp_mean_mag`, $G_{\rm RP} =$ `phot_rp_mean_mag`,

1. $\chi \equiv \sqrt{\chi^2/n}$, $\chi < 1.2\max(1, \exp{-0.2}(G - 19.5))$
2. $1.0{+}0.015(G_{\rm BP}{-}G_{\rm RP})^2 <$ `phot_bp_rp_excess_factor` $< 1.3 + 0.06(G_{\rm BP}{-}G_{\rm RP})^2$.

These quality cuts ensure a good astrometric solution. We also exclude a handful of stars whose parallaxes or radii that we derive below disagree between asteroseismology and *Gaia* at the 5σ level. We do not explicitly exclude negative parallaxes, and our analysis method described in the next section does not require positive parallaxes. However, after the above cuts, only positive parallaxes remain.

3. Methods

A star's radius, R, is related to its parallax, ϖ, through its effective temperature, $T_{\rm eff}$, and its bolometric flux, F, via

$$\begin{aligned}\varpi(F, T_{\rm eff}, R) &= F^{1/2}\sigma_{\rm SB}^{-1/2}T_{\rm eff}^{-2}R^{-1}\\ &= f_0^{1/2}\,10^{-1/5(m+{\rm BC}(b,T_{\rm eff})-A_b)}\sigma_{\rm SB}^{-1/2}T_{\rm eff}^{-2}R^{-1},\end{aligned} \quad (1)$$

where $\sigma_{\rm SB}$ is the Stefan–Boltzmann constant; $f_0 = 2.5460 \times 10^{-5}$ erg s^{-1} cm^{-2} is a zero-point factor to convert magnitude into flux and is computed assuming a solar irradiance from Mamajek et al. (2015), $f_0 = 1.361 \times 10^6$ erg s^{-1} cm^{-2}, and an apparent solar bolometric magnitude of $m_{\rm bol} = -26.82$ (using the visual magnitude of the Sun, $V_\odot = -26.76$, and its visual bolometric correction, ${\rm BC}_{V,\odot} = -0.06$; Torres 2010); BC is the bolometric correction, which depends on the photometric bandpass used, b, and the temperature; and A_b is the extinction in that band. One may use this equation to compute a radius from the *Gaia* parallax, or a parallax from an asteroseismic radius. Asteroseismic radii themselves are derived from a radius scaling relation using the asteroseismic properties $\Delta\nu$ and $\nu_{\rm max}$, which represent the typical frequency spacings between acoustic overtone modes in solar-like

[10] A final step allows for, e.g., General Relativity variations.

oscillators and the frequency for which those oscillations are largest:

$$\frac{R}{R_\odot} \approx \left(\frac{\nu_{\rm max}}{\nu_{\rm max,\odot}}\right)\left(\frac{\Delta\nu}{\Delta\nu_\odot}\right)^{-2}\left(\frac{T_{\rm eff}}{T_{\rm eff,\odot}}\right)^{1/2}. \quad (2)$$

The published *Gaia* radii depend on an estimate of the flux of the star, and not just the parallax. Because the published *Gaia* radii are computed without taking into account extinction, the published *Gaia* radii are systematically too small. To remove this known effect, we calculate our own radii using *Gaia* parallaxes, according to Equation (1) with visual photometry, which we refer to henceforth as *Gaia* radii.

One can see that Equation (1) suggests that for our comparison between *Gaia* and asteroseismic results, we can either use *Gaia* parallaxes with a flux and a temperature to yield a *Gaia* radius, or alternatively use the asteroseismic radius along with a flux and temperature to compute a parallax. In the following, we consider both approaches.

3.1. Parallax Comparison

It is simplest to identify a zero-point offset in the *Gaia* parallaxes in parallax space—i.e., by converting asteroseismic radii into asteroseismic parallaxes. The following equations represent our assumptions that the observed *Gaia* parallaxes are offset from the true parallax, ϖ, by a constant global value, c, and are subject to Gaussian measurement/modeling noise (Equation (3)); and the observed asteroseismic radii are unbiased measurements of the true parallax, subject to Gaussian noise (Equation (4)):

$$\hat{\varpi}_{Gaia} \sim \mathcal{N}(\varpi - c, \sigma^2_{\varpi_{Gaia}}) \quad (3)$$

$$\hat{\varpi}_{\rm seis} \sim \mathcal{N}(\varpi, \sigma^2_{\varpi_{\rm seis}}). \quad (4)$$

The variance due to measurement/modeling noise for the observed *Gaia* parallaxes is taken from the `parallax_error` field of the *Gaia* catalog; the variance for the observed asteroseismic parallax is computed by applying standard propagation of error to Equation (1), thereby treating the fractional variance in asteroseismic parallax as the appropriate weighted sum in quadrature of the fractional variances of flux, temperature, and asteroseismic radius. In our analysis, we ignore objects that were 5σ outliers in parallax difference.

Equations (3) and (4) propose that the difference between asteroseismic and *Gaia* parallax scales is due to a constant zero-point error in the *Gaia* parallaxes, like the one found by the *Gaia* team. Astrophysically, this is a reasonable model, given that errors in the three pillars underpinning the asteroseismic parallax scale—the scaling relation radius, temperature, and bolometric correction—result in fractional and not additive errors in the asteroseismic parallax (Equation (1)). It is for this reason that we have treated the random uncertainties in asteroseismic parallax fractionally. By extension, this means that in the presence of systematic errors in the asteroseismic parallax, the observed parallaxes would be fractionally different from the true parallax. This is to be contrasted with the *Gaia* parallax case: L18 expect systematic errors in the *Gaia* parallax to be additive, not fractional, due to the nature of the mathematical degeneracy that L18 proposes may produce the constant global *Gaia* parallax zero-point error they find. Instead, global problems in the radius or temperature scale, for instance, would be parallax- and therefore distant-dependent effects. Indeed, in the presence of systematic errors, the asteroseismic parallax would generally be incorrect by a fractional factor, f, meaning that Equations (3)–(4) would read

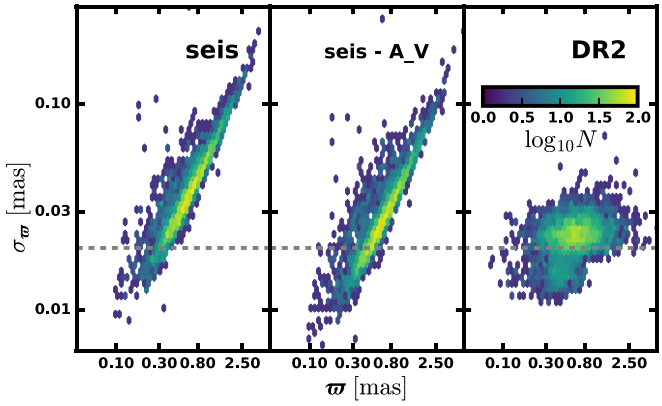

Figure 2. Asteroseismic parallax uncertainty as a function of asteroseismic parallax with and without A_V uncertainty included ("seis," "seis-A_V") , and *Gaia* parallax uncertainty as a function of Gaia parallax ("DR2") for our main sample. The color scale indicates the number of points per hexagonal cell. The horizontal dashed line indicates an error of 0.02 mas to guide the eye. Note the logarithmic scale on both axes.

$$\hat{\varpi}'_{Gaia} \sim \mathcal{N}(\varpi - c, \sigma^2_{\varpi_{Gaia}}) \quad (5)$$

$$\hat{\varpi}'_{\rm seis} \sim \mathcal{N}(f\varpi, f^2\sigma^2_{\varpi_{\rm seis}}). \quad (6)$$

The observed parallax difference, $\hat{\varpi}'_{\rm seis} - \hat{\varpi}'_{Gaia}$ would also not be described by a simple additive offset, c, but rather by a parallax-dependent function, $(f-1)\varpi_{\rm seis} + c$.

Equations (5) and (6) suggest a test of our assumption that the offset is due to *Gaia* and not asteroseismology errors: parallax-dependent offsets could indicate systematic errors in the asteroseismic parallaxes. In the analysis to follow, we therefore investigated the parallax offset as a function of parallax and other observables, and as a function of different populations, which might indicate more subtle, population-dependent asteroseismic parallax errors. We find no strong evidence for a problem with either the radius scale or the temperature scale, and we place limits on the effects of bolometric correction systematics as well. We thus take c to be an estimate in the *Kepler* field of the global *Gaia* parallax error found in Lindegren et al. (2018) and Arenou et al. (2018).

The dominant assumption in our analysis is that the asteroseismic parallax/radius scale is the absolute one, and the *Gaia* parallax/radius scale deviates from this. We examine in more detail this assumption that the asteroseismic parallaxes are *accurate* in Section 5. Apart from the matter of accuracy, our present analysis benefits from the exquisite precisions of our asteroseismic parallaxes. If the asteroseismic parallax precisions were worse than those from *Gaia*, the uncertainty on our inferred global offset c would suffer. However, this is not the case. If taken at face value, Figure 2 demonstrates that the asteroseismic parallaxes for our sample are at least as precise as that of the *Gaia* parallaxes, if not more. In fact, we have reason to suspect that the *Gaia* parallax uncertainties are underestimated. For stars with $G < 12$, the uncertainties appear well behaved, thanks to a postprocessing inflation to the formal uncertainties the *Gaia* team applied (L18). However, through comparisons to literature distances, Arenou et al. (2018) have

pointed out that parallax uncertainties are significantly underestimated—by as much as 40% for $13 < G < 15$ (the regime in which 15% of our sample lives). For the purposes of our analysis, we have assumed that the formal uncertainties on *Gaia* parallaxes are accurate. On the asteroseismic side, our asteroseismic parallaxes have individual precisions of about 5%, meaning that our entire sample of ∼3500 stars naively could constrain c to better than 0.1% or 0.5 μas. This may very well be an overestimate of our asteroseismic parallax uncertainties, as we have reason to suspect that the A_V uncertainties are inflated, which increases the asteroseismic parallax uncertainties ("seis" versus "seis—A_V" in Figure 2). Indeed, we find no evidence for an increase in scatter in *Gaia* radius at fixed asteroseismic radius for stars with larger formal A_V uncertainties. We investigate the impact of A_V on our results in Section 5.1.1, and find that our result is robust across different extinction regimes. For the purposes of this work, then, we conservatively assume the Bayesian uncertainty estimates of A_V from Rodrigues et al. (2014).

We find that the goodness-of-fit, as quantified by χ^2/dof, of our inferred parallax offset between asteroseismology and *Gaia* depends crucially on allowing for spatially correlated errors according to the estimate for the spatial covariance matrix of the *Gaia* parallaxes in Equation (16) of L18. We write the covariance of the *Gaia* and asteroseismic parallax difference between two stars i and j separated by an angular distance, θ_{ij}, as $C_{ij}(\theta_{ij}) = f(\theta_{ij}) + \delta_{ij}\sigma^2_{\varpi_{Gaia},i} + \delta_{ij}\sigma^2_{\varpi_{\rm seis},i}$, where $f(\theta_{ij})$ describes the spatial correlations in *Gaia* parallax error, and δ_{ij} is the Kronecker delta function. L18, using their quasar reference sample, find $f(\theta_{ij}) = a\exp(-\theta_{ij}/b)$, with $a = 135\ \mu{\rm as}^2$ and $b = 14°$. This covariance function was fit across the entire sky, and models the covariance at the largest scales well. However, because we wish to characterize the zero-point offset in the *Kepler* field specifically, we can ignore the covariance at the largest scales, and only consider the covariance on scales smaller than the *Kepler* field. We tried three approaches for quantifying the small-scale spatial correlations: (1) adopting the exponential form from L18 as is ($a = 135\ \mu{\rm as}^2$ and $b = 14°$); (2) adopting the same exponential form from L18, but with $a = 1500\ \mu{\rm as}^2$ and $b = 0.^\circ11$ (the angular scale is taken from fits to TGAS parallax covariance from Zinn et al. (2017), and a is chosen to reproduce the smallest-scale behavior in the observed covariance in L18); and (3) ignoring spatial correlations altogether. We settle on the L18 covariance function (1), as it yields the best goodness-of-fit, and consider the average spread of the best-fitting c in these methods as a systematic error of $\pm1\ \mu$as on c due to the choice of spatial covariance. This is a minimum estimate of the systematic error on the offset, and we discuss additional systematic errors on the offset due to the bolometric correction, temperature scale, and radius scale in Section 5.1.

Conveniently, the *Kepler* field is easily subdivided into small patches that correspond to the spacecraft "modules" that house the CCDs on which a star's image is recorded for a given quarter.[11] We choose therefore to consider the errors on the parallax for stars of a given module to be independent of those of stars on every other module. As we are ignoring correlations in parallax on the largest scales, this is justified, and roughly amounts to truncating our covariance function at angular scales larger than the module size of $\sim2.^\circ4$. Our results are not sensitive to the details of the module-level truncation, which we discuss in Section 5.1.1.

Ignoring correlations among the observables ($T_{\rm eff}$, $\Delta\nu$, $\nu_{\rm max}$, A_V, g, and r) yields a likelihood function for N stars on each module, m:

$$\mathcal{L}_m(c|\hat{\varpi}_{Gaia}, \hat{T}_{\rm eff}, \hat{\Delta\nu}, \hat{\nu}_{\rm max}, \hat{A}_V, \hat{g}, \hat{r}, \hat{BC}) = \frac{1}{\sqrt{(2\pi)^N|C|}} \times \exp\left[-\frac{1}{2}(\boldsymbol{y}-\boldsymbol{x})^{\rm T}C^{-1}(\boldsymbol{y}-\boldsymbol{x})\right], \tag{7}$$

where

$$\boldsymbol{y} \equiv \hat{\varpi}_{\rm seis}(\hat{T}_{\rm eff}, \hat{\Delta\nu}, \hat{\nu}_{\rm max}, \hat{A}_V, \hat{g}, \hat{r}, \hat{BC})$$
$$\boldsymbol{x} \equiv \hat{\varpi}_{Gaia} + c,$$

and where the flux has been computed using g and r in combination with A_V and a V-band bolometric correction that depends on $T_{\rm eff}$ from Flower (1996), BC(V, $T_{\rm eff}$), on which we assign a 3% uncertainty. This is lower by one percent than the formal uncertainty on the BC for a typical star in our sample, but the precise uncertainty adopted on the BC does not significantly change our result. The conversion from g and r to a V-band magnitude is taken from Lupton (2005).[12] The uncertainty introduced from the transformation is negligible compared to the uncertainties on A_V, given the 1% uncertainties on g and r. In addition to the random uncertainties of A_V, g, r, and $T_{\rm eff}$, the asteroseismic parallax uncertainty, $\sigma^2_{\varpi_{\rm seis}}$, which enters on the diagonal of C (see discussion of parallax covariance, above), also incorporates the random uncertainties on $\Delta\nu$ and $\nu_{\rm max}$. In this way, random uncertainties on both *Gaia* and asteroseismic parallaxes are accounted for, as are spatially correlated systematic errors on *Gaia* parallaxes from the non-diagonal entries of C. We ignore other forms of correlations among the observables that enter into the right-hand side of Equation (1), for instance between g and r; these are small corrections to the final uncertainty in the asteroseismic parallax—for instance, accounting for the correlation between the ${T_{\rm eff}}^{-2}$ term in Equation (1) and the temperature dependence of asteroseismic radius, R (Equation (2)), inflates the uncertainty on individual asteroseismic parallaxes by ∼10%, which negligibly impacts the inferred central values or uncertainties of our final result.

Because L18 points out color and magnitude dependences of the parallax zero-point error in their comparison quasar sample, we build upon this model by adding *Gaia* color and magnitude terms:

$$P_m(c, d, e|\hat{\varpi}_{Gaia}, \hat{T}_{\rm eff}, \hat{\Delta\nu}, \hat{\nu}_{\rm max}, \hat{A}_V, \hat{g}, \hat{r}, \hat{BC}, \hat{G}, \hat{\nu}_{\rm eff}) \propto \exp\left[-\frac{1}{2}(c-\bar{c})^2/\sigma_c^2/M\right] \times \frac{1}{\sqrt{(2\pi)^N|C'|}}\exp\left[-\frac{1}{2}(\boldsymbol{y}-\boldsymbol{x})^{\rm T}C'^{-1}(\boldsymbol{y}-\boldsymbol{x})\right], \tag{8}$$

[11] The spacecraft turns by 90° each quarter, so that the same star is found on one of four modules over the 16-quarter *Kepler* mission.

[12] http://www.sdss3.org/dr8/algorithms/sdssUBVRITransform.php

where

$$\boldsymbol{y} \equiv \hat{\varpi}_{\rm seis}(\hat{T}_{\rm eff},\, \hat{\Delta\nu},\, \hat{\nu}_{\rm max},\, \hat{A}_V,\, \hat{g},\, \hat{r},\, \hat{BC})$$
$$\boldsymbol{x} \equiv \hat{\varpi}_{Gaia} \;+ c + d(\hat{\nu}_{\rm eff} \;- 1.5) + e(\hat{G} - 12.2).$$

This is our final model, which we assume for all our results unless otherwise stated, and which describes the Bayesian posterior probability of the parameters $\mu_m \equiv \{c, d, e\}$, for each module, m, out of a total of $M = 21$ modules. We use a prior on c based on our best-fitting value for the model with no color or magnitude terms or spatial correlations in parallax, $\bar{c} \approx 55\ \mu$as, and a width approximately twice its uncertainty, $\sigma_c \approx 1.5\ \mu$as, as reported in the next section, although our results are insensitive to including the prior or having an implicit flat improper prior for c. This prior is also used in the parallax space comparisons described in Section 5.1. Here, the covariance includes two additional terms along the diagonal: $C_{ij}^{'} = C_{ij} + \delta_{ij} d^2 \sigma^2_{\nu_{\rm eff},i} + \delta_{ij} e^2 \sigma^2_{iG}$, with $\sigma_{i\nu_{\rm eff}}$ as the `astrometric_pseudo_colour_error` field for star i from the DR2 catalog, and σ_{iG} the uncertainty on G, which we assign as 1%, which reflects the 10 mmag level systematics in *Gaia* photometry for $G > 3$ based on comparison to external catalogs (Evans et al. 2018). We assign the values 12.2 and 1.5, which are the medians of G and $\nu_{\rm eff}$ for our sample, to center the magnitude- and color-dependent terms. In this way, a star with the median $\nu_{\rm eff}$ of 1.5 and the median G-band magnitude of 12.2 would have no magnitude or color correction. They are therefore not parameters in this model. We have used the astrometric pseudocolor here as it should be more correlated with the astrometric properties of the *Gaia* DR2 solution than $G_{\rm BP}$–$G_{\rm RP}$. Arenou et al. (2018) indeed finds that the *Gaia* quasar parallax zero-point is more sensitive to $\nu_{\rm eff}$ than $G_{\rm BP}$–$G_{\rm RP}$ (see their Figure 18).

In what follows, c is referred to as a constant global offset to stress that it is a mean offset present in all *Gaia* parallaxes in the *Kepler* field. The global term, c, is larger in magnitude for our sample than other higher-order contributions to the *Gaia* parallax offset, which we model as dependent on color, magnitude, and spatial extent. Additional color-, magnitude-, or spatially dependent terms in the offset are taken into account in our model, but we attempt to make a distinction between the "constant" or "global" offset, c, that applies to all *Gaia* parallaxes in our sample, and the more general parallax offset appropriate for a particular star, given its color, magnitude, and position on the sky.

Because we can consider each module independently, we estimate c for each module, and combine their values assuming they are described by a Gaussian around true values, estimated to be $\hat{\mu}_M$, with covariance, $\hat{\Sigma}_M$, which we estimate as

$$P_M(c, d, e) \propto \Pi_{m=0}^{M} P_m(c, d, e) \propto \mathcal{N}(\hat{\mu}_M, \hat{\Sigma}_M), \tag{9}$$

where

$$\hat{\Sigma}_M = \left(\sum_{m=0}^{M} \hat{\Sigma}_m^{-1} \right)^{-1} \tag{10}$$

$$\hat{\mu}_M = \hat{\Sigma}_M \left(\sum_{m=0}^{M} \hat{\Sigma}_m^{-1} \hat{\mu}_m \right), \tag{11}$$

where each module's best-fitting parameters, $\hat{\mu}_m$, and covariance matrices, $\hat{\Sigma}_m$, are estimated from Markov chain Monte Carlo (MCMC) using `emcee` (Foreman-Mackey et al. 2013; see Neiswanger et al. 2013 for this and other more elaborate MCMC parallelization procedures). The posterior distributions for an example set of module-level parameters, $\hat{\mu}_m$, are shown in Figure 3.

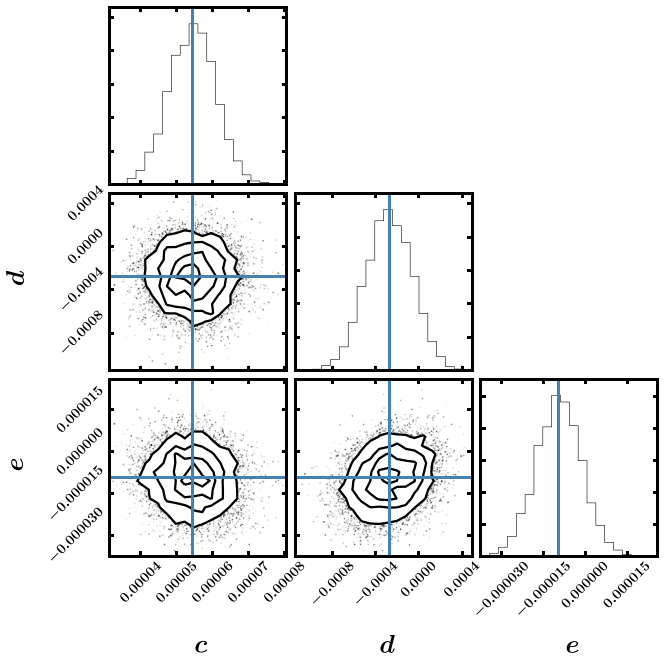

Figure 3. The posterior distributions of the parameters for our parallax offset model (Equation (8)) for a single *Kepler* module. We combine the posteriors for each module to yield our final best-fitting parameters according to Equation (9).

3.2. Radius Comparison

We also investigate the *Gaia* offset in inverse radius space. In this case, the error budget is allocated differently because the *Gaia* radius inherits uncertainty from combining ϖ_{Gaia} with the flux and temperature to yield a radius.

We opt to work in terms of inverse radius, which is directly proportional to parallax, thereby avoiding the bias and high variance when converting the parallax into a distance with $d = 1/\varpi$. (see Bailer-Jones 2015 for thorough discussions of the pitfalls in this approach). This inverted radius formalism also does not require the parallax to be positive, as a negative parallax indicates a noisy estimate of a large radius (small inverse radius). (In our sample, however, the negative parallaxes are filtered out by the conditions listed in Section 2.) The formal uncertainties on the asteroseismic radii of ∼1.5% are such that inverting the asteroseismic radius is well tolerated.

We assume that the observed *Gaia* radius is offset from the true radius through its observed parallax, which is offset by c from the true parallax, ϖ, and that it is subject to measurement/modeling noise (Equation (12)). As we note in the previous section, the offset, c, is applied to the *Gaia* parallax because we interpret it as a systematic error in the *Gaia* parallax and not in the asteroseismic parallax. We also assume that the observed asteroseismic radius is distributed around the true radius, R^{-1},

with known measurement/modeling noise (Equation (13)),

$$\hat{R}_{Gaia}^{-1} \sim \mathcal{N}(\hat{F}^{-1/2}\sigma_{\rm SB}^{1/2}\hat{T}_{\rm eff}^{2}(\varpi - c),\ \sigma_{Gaia,R}^{2} + \sigma_{FT,i}^{2}) \quad (12)$$

$$\hat{R}_{\rm seis}^{-1} \sim \mathcal{N}(R^{-1},\ \sigma_{{\rm seis},R}^{2}), \quad (13)$$

where a hat denotes an observed quantity. The variance of the inverse asteroseismic radius, $\sigma_{{\rm seis},R}^{2}$, is computed according to standard error propagation applied to Equation (2), thus incorporating random uncertainty contributions from $\Delta\nu$, $\nu_{\rm max}$, and APOGEE $T_{\rm eff}$. The variance of the *Gaia* inverse radius is computed according to the standard propagation of error applied to Equation (1), and for clarity has been split into a contribution due to fractional uncertainties in the observed *Gaia* inverse radius due to flux, temperature, and *Gaia* parallax, denoted $\sigma_{Gaia,R}^{2}$, and a smaller contribution due to the offset, c, denoted $\sigma_{FT,i}^{2}$, which is the variance of the quantity $c\hat{F}^{-1/2}\sigma_{\rm SB}^{1/2}\hat{T_{\rm eff}}^{2}$. The *Gaia* radius is computed from the same photometry, BCs, extinctions, and temperatures as the asteroseismic parallax was in the previous section.

We formulate Equations (12) and (13) into a likelihood for our N stars:

$$\begin{aligned}\mathcal{L}(c|\varpi_{Gaia},\ \hat{T}_{\rm eff},\ \hat{\Delta\nu},\ \hat{\nu}_{\rm max},\ \hat{A}_V,\ \hat{g},\ \hat{r},\ \hat{BC}) \\ = \Pi_i (2\pi)^{-N/2}(\sigma_{FT,i}^{2} + \sigma_{{\rm seis},R,i}^{2} + \sigma_{Gaia,R,i}^{2})^{-1/2} \\ \times \exp\left[-\frac{1}{2}(x_i - y_i)^2/(\sigma_{FT,i}^{2} + \sigma_{{\rm seis},R,i}^{2} + \sigma_{Gaia,R,i}^{2})\right],\end{aligned} \quad (14)$$

where

$$\begin{aligned} x_i &\equiv \hat{R}_{{\rm seis},i}^{-1}(\hat{\Delta\nu},\ \hat{\nu}_{\rm max},\ \hat{T}_{\rm eff}) \\ y_i &\equiv \hat{R}_{Gaia,i}^{-1}(\hat{\varpi}_{Gaia},\ \hat{T}_{\rm eff},\ \hat{A}_V,\ \hat{g},\ \hat{r},\ \hat{BC}) \\ &\quad + c\hat{F}(\hat{T}_{\rm eff},\ \hat{A}_V,\ \hat{g},\ \hat{r},\ \hat{BC})^{-1/2}\hat{T}_{\rm eff}^{2}. \end{aligned}$$

Again, we ignore other correlations among observables, for instance, in temperature. This model is used for validating our main model, Equation (8). We do not include spatial correlations in the parallax for this model, and neither do we fit for color or magnitude terms in radius space.

In what follows, we report the uncertainty in c, d, and e from the diagonal of the parameter covariance matrix described above (Equation (10)), $\hat{\Sigma}_M$, and the best-fitting values from $\hat{\mu}_M$, except for the radius space comparison offset, c, (Equation (14)), where we take the mean and standard deviation from our MCMC posteriors.

4. Results

Regardless of the method used, we find a consistent asteroseismology-*Gaia* parallax offset for our *Kepler* RGB sample of $\approx$53 μas. Our main RGB sample yields an offset of 52.8 $\pm$ 2.4 (rand.) $\pm$ 8.6 (syst.) μas, with color and magnitude terms of -150.7 ± 22.7 μas μm and -4.21 ± 0.77 μas mag^{-1}. This result is consistent with that inferred from the radius-based method ($c = 56.3 \pm 0.65$ μas); when fitting c without the color and magnitude terms ($c = 52.9 \pm 0.35$ μas); and when no spatially correlated parallax errors are used ($c = 54.8 \pm 0.66$ μas). We discuss our systematic error term below.

We visualize the offset in parallax as a function of both *Gaia* parallax (Figure 4) and asteroseismic parallax (Figure 5(b)). In these figures, the gray band indicates a model for the parallax offset being a constant equal to c, whereas the purple also takes into account the color- and magnitude-dependent terms. Although it is not evident in these plots, the color- and magnitude-dependent terms are necessary to describe the variability in the offset as a function of various observables, and variations in the offset along these dimensions contribute to the observed scatter away from the gray band in Figures 4 and 5(b). Indeed, it is only by looking at the offset as a function of our other parameters in Figure 6 that we see that the color and magnitude terms are required to explain the data. This is particularly evident of course in $\nu_{\rm eff}$ and G space (Figures 6(e) and (f)), but also notably in $\Delta\nu$ and $\nu_{\rm max}$ space (Figures 6(b) and (c)), where the color and magnitude terms perform better than the global offset. The color term also shows up in the more familiar photometric color space, $G_{\rm BP}$–$G_{\rm RP}$, shown in Figure 6(h). The uptick of the offset for $\varpi_{Gaia} \lesssim 0.2$ mas seen in Figure 4 is likely due to a bias in binned parallax values in the presence of large fractional *Gaia* parallax error (Arenou & Luri 1999; F. Arenou 2019, personal communication).

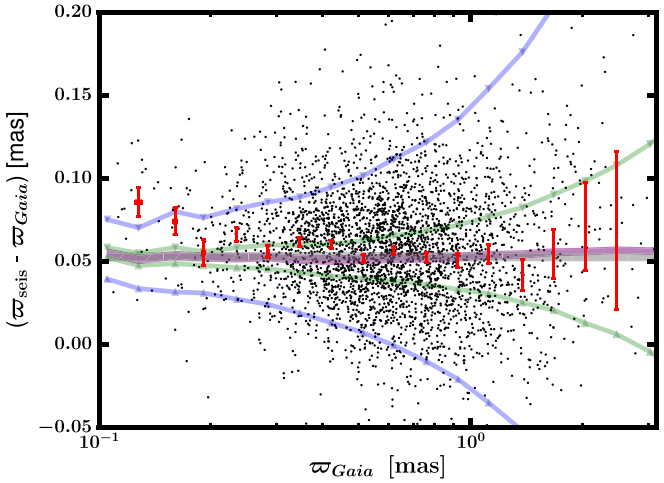

Figure 4. Difference in *Gaia* and asteroseismic parallax as a function of *Gaia* parallax. The observed data are shown in black, along with a binned median (red error bars). The 1σ region for the best-fitting model using only a global offset of c is indicated by the gray band, and one with color and G terms to describe the *Gaia* parallax offset by the purple band (with $\pm1\sigma$ in the global offset, and $\pm0.5\sigma$ in the color and G terms). Shown also are predicted effects from errors of $\pm$100 K in the APOGEE temperature scale (blue) and $\pm$2% in the radius scaling relation (Equation (2); green). See the text for details.

5. Discussion

5.1. Systematic Errors in the Zero-point Offset

Here, we present an estimate for the systematic error on our inferred *Gaia* parallax offset, c, due to systematic errors in the asteroseismic parallax scale we adopt. We want the systematic error to reflect how accurate our reported parallax offset, c, is in an absolute sense. As mentioned in Section 3, three fundamental scales underpin the asteroseismic parallax: a bolometric flux scale set by the bolometric correction; a temperature scale; and a radius scale. Regarding the radius scale, the APOKASC-2 asteroseismic radii have a 1σ systematic error of 0.7% due to the uncertainty in the dynamical open cluster giant mass value that Pinsonneault et al. (2018) adopts; this systematic error of 0.7% in the radius scale naturally accounts for systematic errors in both $\nu_{\rm max}$ and $\Delta\nu$. Regarding temperatures, the IRFM scale, against which

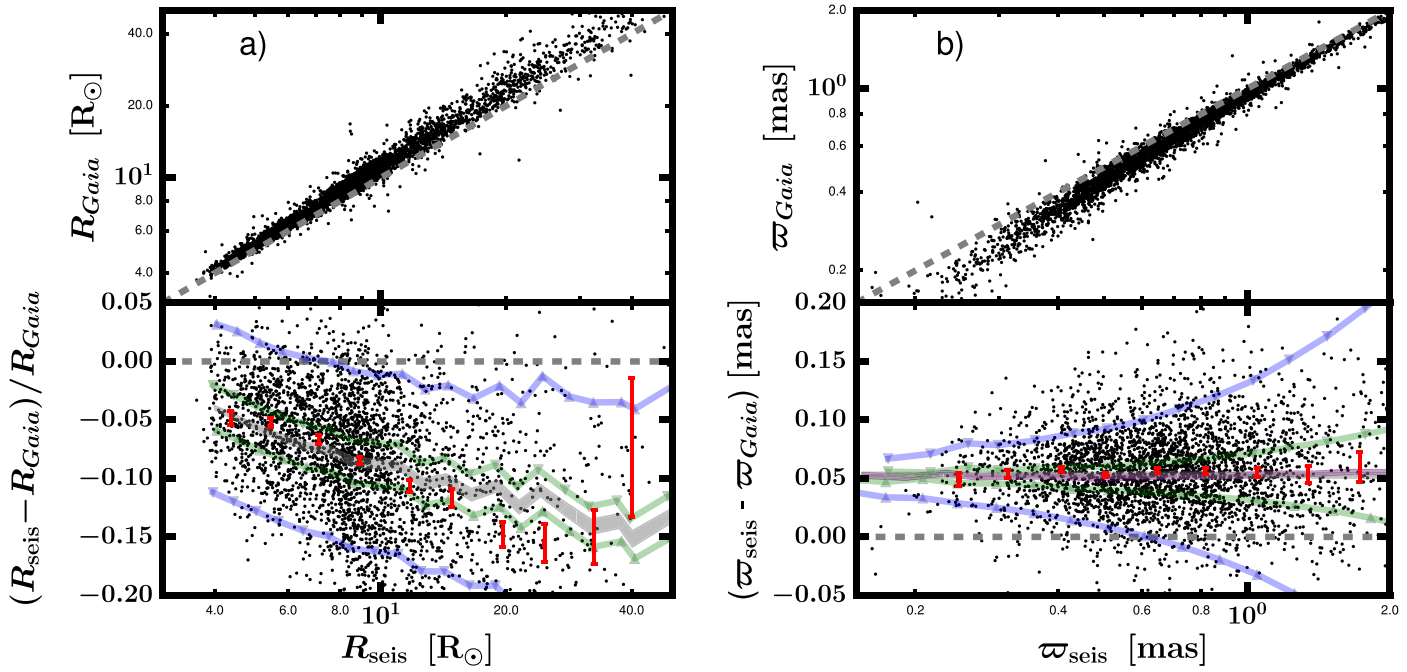

Figure 5. Fractional difference in *Gaia* and asteroseismic radii as a function of asteroseismic radii (a), and difference in *Gaia* and asteroseismic parallax as a function of asteroseismic parallax (b). In the radius panel (a), the gray band indicates the best-fitting 1σ model, which only allows for an offset in the *Gaia* parallax (Equation (14)). In the parallax panel, the purple band indicates a model that allows for color and *G* terms in the *Gaia* parallax offset (Equation (8)), with $\pm1\sigma$ in the global offset, and $\pm0.5\sigma$ in the color and *G* terms. The observed data (black) and binned median (red error bars) are well described by a global offset of *c* (gray band). Shown also are models describing how the binned medians of the data (red error bars) would appear in the presence of systematic errors of ±100 K in the APOGEE temperature scale (blue) and systematic errors of $\pm2\%$ in the radius scaling relation (Equation (2); green). See the text for details.

APOGEE temperatures are calibrated (González Hernández & Bonifacio 2009), agrees with the previously largest application of the IRFM to giants by Alonso et al. (1999) to within ≈43 K, for the metallicity range in which the majority of our sample lies ($-0.4 < [Fe/H] < 0.4$). We therefore adopt 43 K as a 2σ systematic error in the temperature scale. Finally, as we note in Section 5.1.2, our bolometric correction choice induces a systematic error of 5 μas on the inferred offset. A final source of uncertainty is due to the *Gaia* spatial correlation form, which we take as 1 μas in Section 3.1. Taken together, these sources of systematic uncertainty on *c* for the median giant in our sample with $\varpi = 600$ μas and a temperature of 4700 K add fractionally in quadrature to produce an uncertainty in *c* consistent with how parallax scales with radius and temperature (Equation (1)):

$$\sigma_c = 600\ \mu\text{as} \times [(0.007)^2 + (43\ \text{K}/4700\ \text{K})^2 + (5\ \mu\text{as}/600\ \mu\text{as})^2 + (1\ \mu\text{as}/600\ \mu\text{as})^2]^{1/2} = 600\ \mu\text{as} \times 0.014 = 8.6\ \mu\text{as}.$$

We therefore adopt a systematic error on *c* of 8.6 μas. We argue in Section 5.1.2 that significant temperature and radius systematics are not visibly present in the data, and so this systematic error estimate may be conservative.

More subtle errors in our inferred *c* may arise due to population effects. For instance, one may worry that our result could be biased by the distribution of our sample's parallaxes and/or parallax uncertainties. We are also interested in quantifying how sensitive our results are to the evolutionary state of our sample. An obvious test is to analyze RC stars and compare them to our RGB results. Moreover, we would expect certain population effects to map into a spatial dependence in our result. An age and/or metallicity gradient in the distance above the Galactic disk could map out a spatial gradient in our asteroseismic parallaxes, for instance. Extinction is also a strong function of height above the disk, which could affect our inferred fluxes in a spatially dependent way. So although we take into account spatially correlated errors in *Gaia* parallax, we now place limits on any spatial correlations in the asteroseismic parallaxes themselves.

For these reasons, we performed several checks of the offset for different populations in order to estimate any systematic effects biasing our inferred value of *c*, including

1. a high-parallax subsample with $\varpi_{Gaia} > 1$ mas,
2. a high-precision subsample with $\sigma_{\varpi_{Gaia}}/\varpi_{Gaia} < 0.05$,
3. two high-extinction subsamples (one with $\ell < 73°$ and another with $b < 15°$),
4. two low-extinction subsamples (one with $\ell > 73°$ and another with $b > 15°$),
5. a subsample consisting only of RC stars, and
6. a metal-rich ([Fe/H] > 0.2) and a metal-poor ([Fe/H] < −0.2) subsample.

In all of these cases, our parallax space model was used to infer *c* (Equation (8)), and only RGB stars were included (except for the RC subsample, which consisted exclusively of RC stars). The results of the offsets and corresponding reduced χ^2 are tabulated in Table 1. For comparison, our main sample is included as "RGB." The agreement among all these methods is excellent, and we discuss the implications for this agreement across position on sky, extinction, and parallax in the next section.

5.1.1. Population Effects

From Table 1, the only difference of note in the inferred global offset from our fiducial RGB sample is in the high ϖ_{Gaia} subsample, with a disagreement at the 1σ level. The

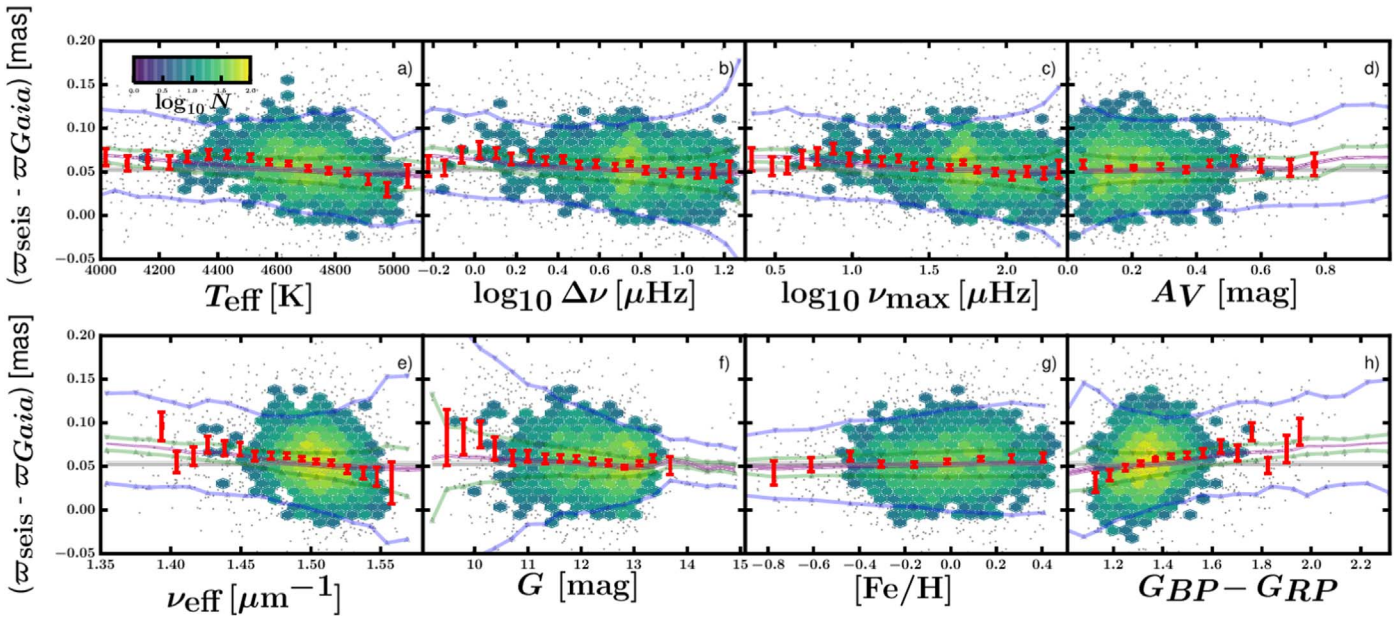

Figure 6. Difference in *Gaia* and asteroseismic parallax as a function of $T_{\rm eff}$ (a), $\Delta\nu$ (b), $\nu_{\rm max}$ (c), A_V (d), $\nu_{\rm eff}$ (e), G (f), [Fe/H] (g), and $G_{\rm BP}$–$G_{\rm RP}$ (h). In general, the observed data (black) and binned median (red error bars) are well described by a global offset of c (gray band), but better described by a model that allows for color and G terms in the *Gaia* parallax offset (purple band; with $\pm1\sigma$ in the global offset, and $\pm0.5\sigma$ in the color and G terms). Shown also are predicted trends due to errors of ±100 K in the APOGEE temperature scale (blue) and $\pm2\%$ in the radius scaling relation (Equation (2); green). See the text for details. Uncertainties on G-band magnitude have been set to 1%. The density of points per bin is denoted by the color bar in panel (a).

Table 1
Terms in the *Gaia* Parallax Zero-point Offset and Their Uncertainties Inferred from Various APOKASC-2 Populations when Fitting with Equation (8)

Sample	c (μas)	d (μas μm)	e (μas mag^{-1})	χ^2/dof	N
$b < 15°$	53.7 ± 2.8	−125.5 ± 26.4	−4.10 ± 0.89	0.946*	2532
$\ell < 73°$	51.6 ± 4.4	−34.9 ± 39.2	−3.56 ± 1.41	1.092*	891
$b > 15°$	53.3 ± 3.2	−191.8 ± 42.2	−4.41 ± 1.48	1.116**	942
$\ell > 73°$	53.1 ± 2.6	−203.8 ± 27.3	−4.57 ± 0.90	0.975	2584
$\varpi_{Gaia} > 1$ mas	46.0 ± 5.7	−255.7 ± 146.3	−13.25 ± 3.82	0.583*****	555
$\sigma_{\varpi Gaia}/\varpi_{Gaia} < 0.05$	53.1 ± 2.3	−215.3 ± 39.7	−5.92 ± 1.00	0.781*****	2640
RC	50.2 ± 2.5	−315.2 ± 49.3	0.79 ± 1.07	0.666*****	2587
[Fe/H] > 0.2	55.3 ± 1.4	−60.2 ± 57.0	−3.20 ± 2.17	0.688*****	587
[Fe/H] < −0.2	54.7 ± 1.4	−160.0 ± 50.5	0.42 ± 1.73	0.977	828
RGB	52.8 ± 2.4	−150.7 ± 22.7	−4.21 ± 0.77	1.007	3475

Note. See the text for details. Asterisks denote the level of discrepancy with the expected χ^2 given the degrees of freedom, $N - 3 - 1$, with one asterisk for each σ in the significance of the discrepancy, capped at 5σ. Our preferred value is from our main "RGB" sample. As noted in the text, a prior on c centered around $c = 55$ μas is adopted, which does not significantly affect the inferred parameters. We estimate a systematic error in c of ±8.6 μas.

different inferred offset among the high ϖ_{Gaia} subsample can be explained by the subsample's bright magnitude distribution, which requires a more substantial magnitude correction term than the fainter RGB sample (-13.25 μas mag^{-1} compared to -4.21 μas mag^{-1}). Indeed, we do see evidence for a nonlinear magnitude-dependent parallax correction from Figure 6(f), where the stars with $G < 10$ cannot be described with a linear magnitude correction. The larger magnitude-dependent parallax correction would then decrease the difference in parallax scales for these bright close stars compared to the difference in parallax scales for the main RGB sample, and result in a smaller inferred parallax offset, c. Note that this implies a shortcoming in our linear magnitude-dependent correction, and does not impugn the c we infer from the broader RGB sample.

There is a statistically insignificant difference of 2.6 μas ± 3.5 μas between the inferred offsets for the RGB and RC subsamples, which indicates that there are not large offsets depending on evolutionary state in the derived asteroseismic parameters. The RC subsample does yield significantly different color and magnitude terms. We can understand the more negative d in the RC subsample than in the RGB sample because the RC is bluer than the RGB, and so it lies in the part of Figure 6(e) where the color trend is nonlinear and more severe ($\nu_{\rm eff} \gtrsim 1.5$). The magnitude term being less negative than that from the RGB sample appears consistent with a scenario in which the RC radii are too large by ∼1%, which would cause a biased trend in the parallax offset as a function of magnitude (green curves in Figure 6(f)), and which would also result in a smaller c in the RC population. This would be consistent with the systematic uncertainties in the RC radius scale being a factor of two greater than in the RGB radius scale (Pinsonneault et al. 2018), corresponding to a median systematic uncertainty of more than 2%. Given the robust calibration of radius for RGB stars, we adopt the parallax zero-point offset estimated from the RGB sample.

The other significant differences in the results of the subsamples in Table 1 lie in a handful of color terms and magnitude terms differing from our RGB solution. Apart from the differing magnitude term for the high ϖ_{Gaia} subsample that we have already discussed, the color terms differ also for the $\ell < 73°$ and $\ell > 73°$ cases. The reason for these differences appears to be that the reddest sources in our sample have a lower parallax offset for $\ell < 73°$ and a larger one for $\ell > 73°$. This means that the color trend is stronger in the $\ell > 73°$ subsample because its red objects have a larger offset than the subsample with $\ell < 73°$. The origin for this difference is unclear, but it might be related to *Gaia* systematics in crowded regions, such as near the Galactic plane (Arenou et al. 2018). Additionally, the metal-rich subsample has a less negative color term, which is due to the sample being narrowly distributed in color space, along a relatively flat part of the color trend at $\nu_{\rm eff} \approx 1.5$. Note that there are no metallicity-dependent effects on c, however, which indicates that there are small, if any, systematics in asteroseismic radii due to metallicity (J. C. Zinn et al. 2019, in preparation).

The too-low reduced χ^2, $\chi^2/{\rm dof}$, for some of the subsamples shown in Table 1 indicates that the error budget for these subsamples is inadequate, although we do achieve an acceptable goodness-of-fit for our main RGB sample. We note that there is uncertainty in our result due to the unknown form of the spatial covariance function for the *Kepler* field, which could bias our reduced χ^2 by changing the best-fitting value and/or changing the effective number of degrees of freedom. We will explore the latter effect in a future work.

Of particular interest is the consistency of the inferred offset in high- and low-extinction regions. We can also see this visually as a flat trend of the parallax difference as a function of extinction in Figure 6(d). The APOGEE temperature scale we have adopted is spectroscopic, and therefore insensitive to extinction, as are asteroseismic frequencies. Fundamentally, then, the agreement across extinction regimes tells us that our combination of extinctions and bolometric correction yields consistent distance estimates. In fields with higher reddening, however, a $K_{\rm s}$-band bolometric correction would likely be a better choice for computing luminosities, given the $K_{\rm s}$ band is insensitive to extinction.

An interesting conclusion to draw from the different spatial subsamples we analyzed is the markedly low variation of the result with spatial position. The four subsamples chosen in low- and high-extinction regions based on position with respect to the Galactic plane agree to within 2.1 μas, and this already small difference is statistically insignificant. On the face of it, this indicates not only that population effects on asteroseismic parallaxes are quite small, but it also indicates that the L18 prescription for spatial correlations in the *Gaia* parallaxes overpredicts the magnitude of spatial correlations for our sample in the *Kepler* field. Instead of a nominal parallax difference of 14 μas for separations of 5° according to Equation (16) of L18, they seem to be at most at the 2 μas level. This observation agrees with our caution that the L18 spatial covariance estimate is expected to be larger than one expected for our sample, given the larger random uncertainties on *Gaia* parallaxes for the sample of quasars on which it is based, which are much bluer and five magnitudes fainter than our giant sample.

To look further into the significance of lower-than-expected levels of spatial correlation, we investigated to what extent edge effects might be introduced by truncating spatial correlations beyond the *Kepler* modules. By not taking into account correlations between stars on neighboring modules, edge effects may contribute to a biased c or one with too-high inferred precision. We therefore analyzed four clusters of three modules, which are located in each of the four corners of the *Kepler* field of view. The module clusters are separated from each other by the width of a module, meaning that the resulting estimates of c are unaffected by truncation of spatial correlations at the module level. The mean c we infer from these four clusters is 51.4, 57.0, 56.6, and 52.8 μas. These clusters deviate at most by 4.2 μas from our final reported value of 52.8 μas, which is well within our systematic error budget of 8.6 μas. This indicates that our module-level truncation of the spatial correlations does not bias our result or error budget, and confirms the markedly low spatial variation on scales larger than 5° that we see among our extinction subsamples.

5.1.2. Fidelity of the APOGEE Temperature Scale and the Radius Scaling Relation

As we show in Section 3, a simple fractional modification to our parallax model to describe a systematic asteroseismic radius error leads to a parallax-dependent asteroseismology-*Gaia* parallax difference. Here, we show that neither a radius error of this sort nor a temperature error is consistent with the observed difference in parallax scales. We therefore conclude that the observed parallax difference is consistent with a global systematic error in the *Gaia* parallaxes, with magnitude- and color-dependent terms.

We show in Figures 4–6 what the offset between asteroseismology and *Gaia* would be if the APOGEE temperature scale differed by +100 K (blue curves with upward triangles) and −100 K (blue curves with downward triangles), and if the asteroseismic radii were inflated by 2% (green curves with upward triangles) and deflated by 2% (green curves with downward triangles). The curves represent the median deviation from the nominal best-fitting model (purple band) by perturbing the nominal temperatures or radii. In other words, they indicate the behavior of the parallax difference in the presence of significant systematic errors in the APOGEE temperatures or radius scaling relation. These curves are indeed parallax-dependent, and commensurate with the simple term in Equation (6): temperature (blue curves) and scaling relation (green curves) effects shown in Figure 5(b) are fractional and become more severe for larger parallax. It is clear that none of these systematics can explain the parallax offset that we infer, because Figures 4 and 5(b) show a parallax offset that is essentially flat as a function of parallax.

If Figures 4 and 5(b) demonstrate that systematic errors in temperature or radius cannot cause the observed parallax difference, more subtle, population-dependent temperature or radius errors may still be present, which might be washed out when viewed as a function of parallax alone. In particular, we can use views of the same systematics curves shown in Figure 4 in slices of other observables to evaluate to what extent the color- and magnitude-dependent terms may be caused by systematic errors in temperature or parallax. Figure 6 shows how these radius and temperature systematics play out as a function of the other observables. These systematics curves do show very similar behavior to the observed parallax difference as a function of the observables. In each case, the systematics curves look consistent with the observed parallax difference if they are shifted by a fixed constant amount. None

of these curves, however, as we show in Figures 4 and 5(b), is consistent with the observed parallax offset as a function of parallax, and so these translations are not permissible. Nevertheless, for a relatively small number of stars on the extremes of the parameter space, we could imagine that these translations are permissible, and would simply lead to larger scatter in the parallax difference when viewed as a function of parallax alone. It is therefore interesting to compare the deviations in the systematics curves at the extremes of some of these slices in parameter space to the curvature in the observed parallax difference seen as a function of color and magnitude. The question in this scenario is whether temperature or radius systematics can induce magnitude- or color-dependent trends in the observed parallax difference.

Consider, as an example, the model for the effect of an increase in the radius (green upward triangles), e.g., which can be thought of as a situation where our radii are too large due to radius scaling relation problems. Looking at the parallax difference in the high-$\nu_{\rm eff}$ regime in Figure 6(e), the offset between *Gaia* and asteroseismic parallax actually decreases with increasing $\nu_{\rm eff}$ because of a population effect, whereby stars with larger $\nu_{\rm eff}$ are closer, and thus a fractional increase in radius for high $\nu_{\rm eff}$ stars leads to a larger absolute asteroseismic parallax shift—in the case of too-high radii, their parallaxes are shifted closer to the observed *Gaia* parallaxes (Figure 6(a)). This is the same sense of the observed trend in parallax difference with $\nu_{\rm eff}$, and could therefore appear to contribute to a color term in the *Gaia* parallax offset. However, an increase in radius scale is not consistent with the magnitude-dependent trend: whereas we observe the nominal offset to increase for brighter stars, an increase in radii results in a decrease in parallax offset for the brightest stars—another population effect whereby the brightest stars in APOKASC-2 are the closest (largest parallax), meaning that a fractional increase in radius for these stars leads to the largest absolute parallax shift. We conclude that unexplained trends for $G < 10$ and $G_{\rm BP}$–$G_{\rm RP} < 1.2$ are more consistent with nonlinear color- and magnitude-dependent *Gaia* parallax systematics than temperature or radius systematics.

These same parallax-dependent trends in the systematics curves also appear in Figure 7, which is analogous to Figure 6, but showing the parallax difference when computing the asteroseismic parallax with a $K_{\rm s}$-band bolometric correction. The BC is interpolated from MIST (Choi et al. 2016; Dotter 2016; Paxton et al. 2011, 2013, 2015) BC tables in metallicity, gravity, and temperature. The tables are constructed using the C3K grid of 1D atmosphere models (C. Conroy et al. 2019, in preparation; based on ATLAS12/SYNTHE; Kurucz 1970, 1993). We use the asteroseismic gravity in combination with temperature and metallicity from the APOKASC-2 catalog for this BC. We see that the effects of a systematic temperature error are significantly reduced compared to the visual bolometric extinction, because for giants, the $K_{\rm s}$ band is on the linear part of the blackbody curve: a large change in temperature will not cause an exponential change in the infrared flux. This bolometric correction approach is also less sensitive to the estimate of the extinction due to decreased dust scattering in the infrared compared to visual wavelengths. The offset we find using this approach yields a value of 42.4 ± 3.5 μas. Unlike the case when we use a *V*-band BC, the $K_{\rm s}$-band BC appears to produce a parallax-dependent parallax difference that could indicate the presence of a small systematic error in the $K_{\rm s}$ BC. Were we to model this error with a fractional term of the sort we propose in our toy model for systematic radius or temperature errors (Equations (5) and (6)), we would recover a parallax offset that is more consistent with the one found using the *V*-band BC. This difference between *V*-band and $K_{\rm s}$-band BC approaches is therefore a conservative estimate of the error in the parallax offset due to BC: allowing for a fractional term in the parallax difference model would enable a more precise estimate of the offset. We adopt the difference in offset between the $K_{\rm s}$ BC and the *V* BC, 10 μas, as a 2σ systematic error. We have included this addition to the systematic error budget, along with systematic errors due to the temperature scale and the scaling relation radius scale in Section 5.1. That the offset inferred using K_s-band photometry is very similar to the one we infer with *V*-band photometry, even though the *V*-band asteroseismic parallaxes are more sensitive to temperature systematics (compare, e.g., the temperature systematics curves in Figures 7 versus 6), further supports our conclusion that temperature systematics are small. Furthermore, because infrared photometry is insensitive to extinction, the 10 μas 2σ systematic uncertainty we infer from this test also accounts for systematics or correlations in our adopted extinctions.

Looking at the trends in all of these dimensions in this way, there does not seem to be evidence for significant problems in the temperature or APOKASC-2 radius scale that would cause either the global zero-point offset or the magnitude- or color-dependent *Gaia* terms we infer. It is nonetheless possible that much smaller temperature offsets ($\sim$10 K) could exist than we have considered, and still be consistent with the flatness in the parallax offset seen in Figures 4 and 5(b). Regarding small radius systematics, based on work in preparation (J. C. Zinn et al. 2019, in preparation), there seems to be a small systematic error in the asteroseismic radius scale such that asteroseismic radii are slightly larger than *Gaia* radii on the giant branch at a level consistent with the systematic error discussed in Section 5.1. This systematic is in the correct sense to explain why the inferred c using a large parallax sample is marginally smaller than 52.8 μas (Table 1). It is also possible that radius and temperature scale systematics could both be present, operating in different senses to shift the inferred zero-point by a small amount while canceling the parallax-dependent offset behavior seen in the systematics curves. In any event, the systematic error in our inferred offset accounts for such possibilities.

5.2. Possible Evidence for Evolutionary-state-dependent Radius Scaling Relation Errors

As a final word on the matter, we note that the above statements have assumed that any changes to the observed parallax offset by radius scaling relation errors are present at all radii (a constant fractional error). However, breakdowns in the scaling relations are expected to occur for the most evolved giants (Mosser et al. 2013; Stello et al. 2014). The largest sample of giants with asteroseismic and eclipsing binary masses and radii (10) indicate evidence for scaling relations yielding inflated masses and radii (Gaulme et al. 2016), although other results with smaller sample sizes have shown consistency in mass and radius scaling relations (Frandsen et al. 2013; Brogaard et al. 2016). Moreover, interferometric radii for four giants in Huber et al. (2012) do not show evidence for

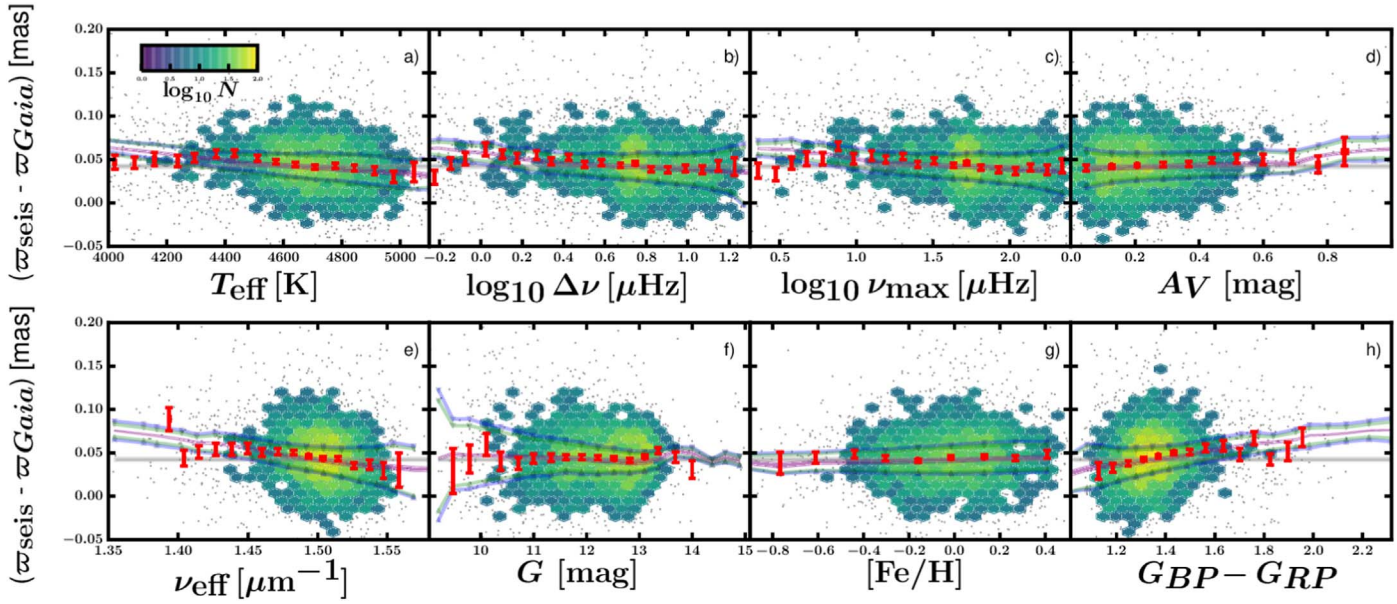

Figure 7. The same as Figure 6, except using a K_s bolometric correction when computing the asteroseismic parallax.

systematics in the scaling relations. It is therefore of great interest to test the fidelity of scaling relations for evolved giants.

In our data, a breakdown in the radius scaling relation for evolved giants would manifest as a decrease in the parallax offset for low-$\Delta\nu$ and ν_{max} stars. We do see hints of this in Figures 6(b) and (c), where there is a downtick in the parallax difference for $\Delta\nu \lesssim 1\ \mu$Hz and $\nu_{max} \lesssim 10\ \mu$Hz. Given the expectation that larger giants would have a stronger breakdown in the radius scaling relation, it might also explain the flattening of the slope in fractional radius difference above $R_{seis} \sim 20\ R_\odot$, compared to our model (Figure 5(a)). However, because larger stars are cooler, this effect may be degenerate with a nonlinear *Gaia* parallax error, where indeed we see that our linear model in color space cannot simultaneously describe the data for cool stars with $\nu_{eff} \lesssim 1.45\ \mu m^{-1}$ and the hotter stars with $\nu_{eff} \gtrsim 1.45\ \mu m^{-1}$ in Figure 6(e); the linear color term cannot precisely fit the whole trend in temperature space in Figure 6(a) either. We cannot discriminate at this point between a scaling relation problem or a color-dependent *Gaia* parallax offset term that our linear model cannot describe. We emphasize, however, that any hints at a scaling relation breakdown only concern interpreting small residuals at the extremes (in color, radius, distance, etc.) of our APOKASC-2 parameter space. We stress that the global *Gaia* parallax offset we report is not consistent with being caused by temperature or scaling relation errors, and neither are the main trends in color and magnitude in the regimes where the bulk of our data lie.

6. Conclusions

With a sample of nearly 3500 first-ascent giants in the APOKASC-2 catalog, we infer a systematic zero-point in the *Gaia* parallaxes of $\varpi_{seis} - \varpi_{Gaia} = 52.8 \pm 2.4$ (rand.) $\pm$ 8.6 (syst.) $-$ $(150.7 \pm 22.7)(\nu_{eff} - 1.5) - (4.21 \pm 0.77)(G - 12.2)\ \mu$as, in the sense that *Gaia* parallaxes are too small. All indications are that the zero-point offset depends on position, magnitude, and color (L18), so we do not advise using our model out-of-the-box. Our work does, however, serve as a useful reference for other studies that need to account for the zero-point offset in their work.

We have confidence in our result because of agreement with the global zero-point parallax error of 29 μas that L18 finds for a sample of nearly 600,000 quasars from AllWISE (Secrest et al. 2015), in the same sense that we find. Although our global offset is larger in an absolute sense than that found by L18, it is consistent with the range of zero-point offsets between $\approx$10 and 100 μas (also in the sense that *Gaia* parallaxes are too small) noted by the *Gaia* team (Arenou et al. 2018). This quoted range was determined from a census that was applied to more than 200,000 stars from 29 sources, ranging from *Hipparcos* (van Leeuwen 2007) to the spectrographic survey LAMOST (Luo et al. 2015). Several independent studies have also corroborated our findings (Groenewegen 2018; Muraveva et al. 2018; Riess et al. 2018; Stassun & Torres 2018; Graczyk et al. 2019; Hall et al. 2019; Khan et al. 2019; Leung & Bovy 2019; Schönrich et al. 2019; Xu et al. 2019), and our global offset is formally statistically consistent with nine of these, while one finds a global offset lower by 2σ (Graczyk et al. 2019), and which, like the L18 results, is a zero-point that has been averaged over the whole sky. Regarding this point, we note that Figure 7 in L18, which shows the global error in the AllWISE quasar sample as a function of ecliptic latitude, suggests that the *Kepler* field, at $\sim$64°, should exhibit a higher error ($\sim$50 μas) than the rest of the sky. We also appear to find the same sign in the magnitude- and color-dependent offset terms as was suggested by Figure 7 of L18.

We conclude the following:

1. For studies using *Gaia* parallaxes of populations of red, bright stars in the *Kepler* field, our estimate of $\varpi_{seis} - \varpi_{Gaia} = 52.8 \pm 2.4$ (rand.) $\pm$ 8.6 (syst.) $-$ $(150.7 \pm 22.7)(\nu_{eff} - 1.5) - (4.21 \pm 0.77)(G - 12.2)\ \mu$as is probably valid, given the various tests provided in Section 5. In our sample, which has a range of $\sim$0.2 in ν_{eff} and spans $\sim$4 mag, the color and magnitude terms are appreciable. We have assigned a systematic error of $\pm$8.6 μas on the global offset due to our bolometric

correction, choice of spatial correlation form for *Gaia* parallaxes, and systematics in our temperature and radius scales.
2. The parallax offsets we infer are not consistent with being due to significant systematic errors in the temperature or radius scale used to compute the asteroseismic parallax, and are in agreement with both the global and the magnitude- and color-dependent parallax errors reported by the *Gaia* team (Arenou et al. 2018; Lindegren et al. 2018).
3. There are only insignificant differences in the *Gaia* zero-point offset due to extinction in the *Kepler* field, and due to population effects (e.g., RGB versus RC).
4. Our spatial covariance model of the DR2 parallaxes in the *Kepler* field likely needs revision, which we will quantify in future work. At this point, there are uncertainties on the parallax zero-point offset because we do not know the precise nature of the spatial correlations, which are at least ± 1 μas.
5. Small trends in the data that our *Gaia* parallax model does not explain are suggestive of the need for a nonlinear treatment of the magnitude and color dependence of the *Gaia* parallax offset. However, these trends appear preferentially for $G < 10$ and $G_{\rm BP}$–$G_{\rm RP} < 1.2$, where relatively few stars exist in our sample, and as such, we leave such an advanced treatment to other work.

In this work, we did not attempt to map out the fidelity of the radius scaling relation, although this is possible in principle, given the difference in trend that a parallax error and a radius error induce on the data. We will investigate this and estimate the spatial dependence of *Gaia* parallax errors in a forthcoming paper on tests of scaling relations as a function of evolutionary state.

M.H.P. and J.Z. acknowledge support from NASA grants 80NSSC18K0391 and NNX17AJ40G. D.H. acknowledges support by the National Science Foundation (AST-1717000) and the National Aeronautics and Space Administration under Grants NNX14AB92G and NNX16AH45G issued through the *Kepler* Participating Scientist Program and the K2 Guest Observer Program. D.S. is the recipient of an Australian Research Council Future Fellowship (project number FT1400147). Parts of this research were conducted by the Australian Research Council Centre of Excellence for All Sky Astrophysics in 3 Dimensions (ASTRO 3D), through project number CE170100013.

This project was developed in part at the 2019 Santa Barbara *Gaia* Sprint, hosted by the Kavli Institute for Theoretical Physics at the University of California, Santa Barbara. This research was supported in part at KITP by the Heising-Simons Foundation and the National Science Foundation under grant No. NSF PHY-1748958.

This work has made use of data from the European Space Agency (ESA) mission *Gaia* (https://www.cosmos.esa.int/gaia), processed by the *Gaia* Data Processing and Analysis Consortium (DPAC, https://www.cosmos.esa.int/web/gaia/dpac/consortium). Funding for the DPAC has been provided by national institutions, in particular the institutions participating in the *Gaia* Multilateral Agreement.

Funding for the Sloan Digital Sky Survey IV has been provided by the Alfred P. Sloan Foundation, the U.S. Department of Energy Office of Science, and the Participating Institutions. SDSS acknowledges support and resources from the Center for High-Performance Computing at the University of Utah. The SDSS website is www.sdss.org. SDSS is managed by the Astrophysical Research Consortium for the Participating Institutions of the SDSS Collaboration including the Brazilian Participation Group, the Carnegie Institution for Science, Carnegie Mellon University, the Chilean Participation Group, the French Participation Group, Harvard Smithsonian Center for Astrophysics, Instituto de Astrofsíca de Canarias, The Johns Hopkins University, Kavli Institute for the Physics and Mathematics of the Universe (IPMU)/University of Tokyo, Lawrence Berkeley National Laboratory, Leibniz Institut für Astrophysik Potsdam (AIP), Max-Planck-Institut für Astronomie (MPIA Heidelberg), Max-Planck-Institut für Astrophysik (MPA Garching), Max-Planck-Institut für Extraterrestrische Physik (MPE), National Astronomical Observatories of China, New Mexico State University, New York University, University of Notre Dame, Observatório Nacional/MCTI, The Ohio State University, Pennsylvania State University, Shanghai Astronomical Observatory, United Kingdom Participation Group, Universidad Nacional Autónoma de México, University of Arizona, University of Colorado Boulder, University of Oxford, University of Portsmouth, University of Utah, University of Virginia, University of Washington, University of Wisconsin, Vanderbilt University, and Yale University.

ORCID iDs

Joel C. Zinn https://orcid.org/0000-0002-7550-7151
Marc H. Pinsonneault https://orcid.org/0000-0002-7549-7766
Daniel Huber https://orcid.org/0000-0001-8832-4488
Dennis Stello https://orcid.org/0000-0002-4879-3519

References

Alonso, A., Arribas, S., & Martínez-Roger, C. 1999, A&AS, 139, 335
Andrae, R., Fouesneau, M., Creevey, O., et al. 2018, A&A, 616, A8
Arenou, F., & Luri, X. 1999, in ASP Conf. Ser. 167, Harmonizing Cosmic Distance Scales in a Post-HIPPARCOS Era, ed. D. Egret & A. Heck (San Francisco, CA: ASP), 13
Arenou, F., Luri, X., Babusiaux, C., et al. 2018, A&A, 616, A17
Bailer-Jones, C. A. L. 2015, PASP, 127, 994
Bedding, T. R., Huber, D., Stello, D., et al. 2010, ApJL, 713, L176
Borucki, W. J., Koch, D., Basri, G., et al. 2010, Sci, 327, 977
Brogaard, K., Jessen-Hansen, J., Handberg, R., et al. 2016, AN, 337, 793
Brown, T. M., Gilliland, R. L., Noyes, R. W., & Ramsey, L. W. 1991, ApJ, 368, 599
Brown, T. M., Latham, D. W., Everett, M. E., & Esquerdo, G. A. 2011, AJ, 142, 112
Casertano, S., Riess, A. G., Bucciarelli, B., & Lattanzi, M. G. 2017, A&A, 599, A67
Choi, J., Dotter, A., Conroy, C., et al. 2016, ApJ, 823, 102
Davies, G. R., Lund, M. N., Miglio, A., et al. 2017, A&A, 598, L4
De Ridder, J., Barban, C., Baudin, F., et al. 2009, Natur, 459, 398
De Ridder, J., Molenberghs, G., Eyer, L., & Aerts, C. 2016, A&A, 595, L3
Dotter, A. 2016, ApJS, 222, 8
Evans, D. W., Riello, M., De Angeli, F., et al. 2018, A&A, 616, A4
Flower, P. J. 1996, ApJ, 469, 355
Foreman-Mackey, D., Hogg, D. W., Lang, D., & Goodman, J. 2013, PASP, 125, 306
Frandsen, S., Lehmann, H., Hekker, S., et al. 2013, A&A, 556, A138
Gaia Collaboration, Brown, A. G. A., Vallenari, A., et al. 2018, A&A, 616, A1
Gaia Collaboration, Prusti, T., de Bruijne, J. H. J., et al. 2016, A&A, 595, A1
Gaulme, P., McKeever, J., Jackiewicz, J., et al. 2016, ApJ, 832, 121
González Hernández, J. I., & Bonifacio, P. 2009, A&A, 497, 497
Graczyk, D., Pietrzyński, G., Gieren, W., et al. 2019, ApJ, 872, 85
Groenewegen, M. A. T. 2018, A&A, 619, A8

Hall, O. J., Davies, G. R., Elsworth, Y. P., et al. 2019, MNRAS, 486, 3569
Hekker, S., Kallinger, T., Baudin, F., et al. 2009, A&A, 506, 465
Huber, D., Ireland, M. J., Bedding, T. R., et al. 2012, ApJ, 760, 32
Huber, D., Zinn, J., Bojsen-Hansen, M., et al. 2017, ApJ, 844, 102
Jao, W.-C., Henry, T. J., Riedel, A. R., et al. 2016, ApJL, 832, L18
Khan, S., Miglio, A., Mosser, B., et al. 2019, arXiv:1904.05676
Kjeldsen, H., & Bedding, T. R. 1995, A&A, 293, 87
Kurucz, R. L. 1970, SAOSR, 309
Kurucz, R. L. 1993, in ASP Conf. Ser. 44, IAU Coll. 138: Peculiar versus Normal Phenomena in A-type and Related Stars, ed. M. M. Dworetsky, F. Castelli, & R. Faraggiana (San Francisco, CA: ASP), 87
Leung, H. W., & Bovy, J. 2019, MNRAS, 483, 3255
Lindegren, L., Hernández, J., Bombrun, A., et al. 2018, A&A, 616, A2
Lindegren, L., Lammers, U., Bastian, U., et al. 2016, A&A, 595, A4
Lindegren, L., Lammers, U., Hobbs, D., et al. 2012, A&A, 538, A78
Luo, A.-L., Zhao, Y.-H., Zhao, G., et al. 2015, RAA, 15, 1095
Mamajek, E. E., Prsa, A., Torres, G., et al. 2015, arXiv:1510.07674
Michalik, D., Lindegren, L., & Hobbs, D. 2015, A&A, 574, A115
Miglio, A., Brogaard, K., Stello, D., et al. 2012, MNRAS, 419, 2077
Mosser, B., Dziembowski, W. A., Belkacem, K., et al. 2013, A&A, 559, A137
Muraveva, T., Delgado, H. E., Clementini, G., Sarro, L. M., & Garofalo, A. 2018, MNRAS, 481, 1195
Neiswanger, W., Wang, C., & Xing, E. 2013, arXiv:1311.4780
Paxton, B., Bildsten, L., Dotter, A., et al. 2011, ApJS, 192, 3
Paxton, B., Cantiello, M., Arras, P., et al. 2013, ApJS, 208, 4
Paxton, B., Marchant, P., Schwab, J., et al. 2015, ApJS, 220, 15
Pinsonneault, M. H., An, D., Molenda-Żakowicz, J., et al. 2012, ApJS, 199, 30
Pinsonneault, M. H., Elsworth, Y. P., Tayar, J., et al. 2018, ApJS, 239, 32
Riello, M., De Angeli, F., Evans, D. W., et al. 2018, A&A, 616, A3
Riess, A. G., Casertano, S., Yuan, W., et al. 2018, ApJ, 861, 126
Rodrigues, T. S., Girardi, L., Miglio, A., et al. 2014, MNRAS, 445, 2758
Schönrich, R., McMillan, P., & Eyer, L. 2019, MNRAS, tmp, 1390
Secrest, N. J., Dudik, R. P., Dorland, B. N., et al. 2015, ApJS, 221, 12
Sesar, B., Fouesneau, M., Price-Whelan, A. M., et al. 2017, ApJ, 838, 107
Sharma, S., Stello, D., Bland-Hawthorn, J., Huber, D., & Bedding, T. R. 2016, ApJ, 822, 15
Skrutskie, M. F., Cutri, R. M., Stiening, R., et al. 2006, AJ, 131, 1163
Stassun, K. G., & Torres, G. 2016, ApJL, 831, L6
Stassun, K. G., & Torres, G. 2018, ApJ, 862, 61
Stello, D., Compton, D. L., Bedding, T. R., et al. 2014, ApJL, 788, L10
Stello, D., Huber, D., Bedding, T. R., et al. 2013, ApJL, 765, L41
Torres, G. 2010, AJ, 140, 1158
Ulrich, R. K. 1986, ApJL, 306, L37
van Leeuwen, F. 2007, A&A, 474, 653
White, T. R., Bedding, T. R., Stello, D., et al. 2011, ApJ, 743, 161
Wright, E. L., Eisenhardt, P. R. M., Mainzer, A. K., et al. 2010, AJ, 140, 1868
Xu, S., Zhang, B., Reid, M. J., Zheng, X., & Wang, G. 2019, ApJ, 875, 114
Yu, J., Huber, D., Bedding, T. R., et al. 2018, ApJS, 236, 42
Zinn, J. C., Huber, D., Pinsonneault, M. H., & Stello, D. 2017, ApJ, 844, 166